A Computer Vision Approach for Dynamic Tracking of Components in a Nuclear Reactor Core Model

Luiza Dihoru*, Adam J. Crewe, Tony Horseman, Matt Dietz, Olafur Oddbjornsson, Panos Kloukinas, Elia Voyagaki, Colin A. Taylor

University of Bristol, University Walk, Bristol, BS8 1TR, United Kingdom
* Corresponding author: Luiza.Dihoru@bristol.ac.uk

Abstract
The Advanced Gas Cooled Reactors (AGRs) are a vital component of the UK's electricity supply system. Their continued reliable operation is supported by safety cases that include assessments of their seismic resilience to their ultimate lifetimes. These assessments are developed via a complex programme of numerical simulations, physical modelling and shaking table testing. A quarter sized physical model representing a single layer of an AGR graphite core was developed at the University of Bristol (UOB) to test the dynamic response for various core array configurations and seismic excitations. The dynamic displacement response is significant, as displaced components may cause local or general distortions that could theoretically affect the channel shapes and the keying system of an AGR core, with implications on the fundamental functions of the reactor. This paper presents a computer vision approach for component displacement mapping. An infrared vision system and a high-resolution video system were employed to track all the components in the model core during a seismic event. The systems have proven to be fit for purpose, being able to map the position of the array components at a resolution of 0.1mm and to reveal features of response that are useful for understanding the core dynamics. The employed hardware and tracking algorithms are general in nature, hence they are transferrable to other case studies involving multi-body assemblies under dynamic loading.

Keywords: Advanced Gas Cooled Reactor, high resolution video, dynamic tracking, seismic testing

1 Introduction

The Advanced Gas Cooled Reactors (AGR) are significant for the UK's energy security, generating ~17% of the country's electricity. The AGR's continued safe and reliable operations are subject to ongoing review, informed by thorough inspection and monitoring of the actual cores and extensive theoretical, analytical and experimental studies. The AGR cores are assemblies of tubular graphite bricks and interlocking keys designed to fulfil a set of functions that are fundamental to the safe operation of a reactor as they:

i) Provide neutron moderation and thermal inertia
ii) Allow gas flow to ensure adequate cooling of the fuel and core
iii) Allow unimpeded movement of control rods and fuel

Seismic resilience, which is intimately related to the structural performance of the graphite reactor core assembly, has been subject to continual examination by the operators (Neighbour 2007, Neighbour 2013, Flewitt and Wickham 2015). The core component displacement during an earthquake can have a crucial impact on the local and the general distortion of a core, as well as on the channel shapes with implications on control rod system and refuelling system operation. Current international standards require that a nuclear plant should be qualified against at least 0.1 g peak ground acceleration, while the operators require that their AGRs can be safely shut down and held down in the case of a more severe seismic event with a probability of exceedance of 10^{-4} per annum (Dihoru et al 2015).

The seismic capability of the AGRs is currently supported by a set of sophisticated computer models (Kralj et. al. 2005, Koziara and Bićanić 2011) that simulate the core dynamics for a given set of

degradation scenarios. While the existing computer models enable the parameter space to be explored more efficiently, there was a need to provide enhanced validation data for their tuning, hence the need for experimentation. In order to contribute to an appropriate level of confidence in the dependability of the computations, the UOB run a programme of physical model development and shaking table testing spanning over a decade. A phased-approach of physical modelling was carried out, that resulted in the development of a 4x4x8 array ('the Minicore'), a single layer 20-brick-across-array ('the Single Layer Array') and an 8-layer 20-brick-across-array ('the Multi-Layer Array'). All three models are quarter sized models based on an existing AGR core and represent all the geometrical features of the prototype (i.e. scaled bricks and keys, scaled brick-to-brick clearances, rocking features of the fuel bricks, and 'dovetail' shaped keyways). The model components are made from a rigid engineering plastic (acetal). Details of model design, build and testing have been published (Dihoru et al 2015, Dihoru et al 2016, Dihoru et al 2018, Voyagaki et al 2018). The rigs were tested extensively on the earthquake simulator, while computer model simulations were run in parallel. In each of those independent pieces of work, whether experimental or computational, the overall driver was reduction of uncertainty and enhanced understanding of dynamics.

This paper stems from the investigation of component movement in the model cores and the case study under analysis is the Single Layer Array (SLA). The work aims at mapping the displacement response of the array components via computer based vision system tracking. In general, motion tracking is the process of recording the movement of objects by employing tools such as accelerometers, tactile or optical measurement systems. Its purpose is to recreate the three dimensional (3D) trajectory of an object during a dynamic event. Motion tracking started as a photogrammetric analysis tool in biomechanics research in the 1970s and 1980s, and expanded into a wide variety of applications in academic research, sports, computer animation and cinematography (Moeslund & Granum 2001). Its principle of operation consists in tracking acoustic, inertial, LED, magnetic or reflective markers (Vlasic et al 2007, Roetenberg et al 2013, Stenborg & Svensson 2005), or combinations of any of these, attached to the objects in motion. The optical measurement systems employ data captured from image markers to triangulate the 3D position of the object (Kurihara et al 2002, Nakamura et al 2003, Sementille et al 2004). This paper presents a motion capture system that consists of a high speed infrared (IR) system and a high-resolution video (HSV) camera working in conjunction with a computer system to track the movement of the SLA components under dynamic loading. The design, deployment and operation of the motion capture system are detailed here, together with a bespoke tracking algorithm developed at UOB. The tracking data is employed in dynamic behaviour interpretation with relevant applicability to AGR cores. Both the hardware and the software for tracking are not application dependent, hence they can be employed in future multi-body assembly rigs for seismic analysis.

2 . Work Objectives and Aplicability of Research

The SLA test programme was designed to suit the validation needs for the existing computer models for seismic behaviour. Its main aim was the mapping of displacement response across the model core, under seismic conditions of various amplitude and frequency content. Such mapping can reveal patterns in response that can be linked to local or general distortion and/or to key-keyway disengagement. All these aspects can feed into a more comprehensive picture of dynamic behaviour that supports the computer modelling work both qualitatively and quantitatively.

Given the large numbers of components in the SLA model array (~ 1200 components), measuring the displacement via traditional contact transducers (linear variable differential transformers (LVDTs), potentiometric transducers, resistive position transducers, etc.) or via traditional non-contact transducers (laser position transducers, Hall effect sensors, eddy current sensors, etc) would be an unrealistic task. Also, the installation of such transducers and their associated cabling would affect the dynamics of the host components via added inertia (note: the model acetal components are relatively light). Hence, a non-contact wide-coverage tool had to be employed for tracking movement. The system had to suit the following performance requirements:

i) Displacement resolution: 0.1mm
ii) Required field of view: 3000mm x 3000mm (XxY)

iii) Dynamic input range: 0-50 Hz.
iv) Typical dynamic test duration: ~ 15-30s

Table 1 summarizes the experimental work objectives and the applicability of results to AGR prototype behaviour.

Table 1 Work objectives and applicability of results

No.	Activity
1	Development of a motion capture system • Bespoke system settings to fit the application • Bespoke tracking software for the high speed video records • Implementation of motion capture system in the SLA rig
2	Build and test the SLA rig.on the shaking table. Test variables dictated by computer modeller needs: array configuration, input (amplitude, frequency range, orientation).
3	Observations of component interactions under dynamic loading. Qualitative observations of core mechanics.
4	Measurement of displacement for selected array components. Evaluate local and general distortion of the core. Evaluate risk of key-keyway disengagement. Understand damage propagation inside the array. Contribute to understanding of fuel and control rod channel shapes in the prototype core.

The purpose of this paper is to present the tool for component tracking, assess its performance and describe tracking outputs with significance in understanding the core behaviour. The tracking outputs are given only as examples that show the capability of the motion capture tool, while a detailed characterization of the array dynamics will be pursued in a subsequent publication.

3. SLA Physical Model Description

The SLA model array consists of quarter sized lattice bricks, interstitial bricks and loose bearing keys made of acetal. The components' geometries are based on the prototype components of one of the UK's AGR graphite cores with the highest irradiation. The prototype cores consist of 12 layers of graphite bricks that form the fuel channels and the control rod channels. The bricks are arranged in 11-12 rings in the horizontal plane. The overall dimensions of an AGR graphite core are: diameter ~11m, height ~10m, weight >1000tonnes. The quarter sized models' ('the Minicore', the 'Single Layer Array' and the 'Multi-Layer Array') development work has been detailed in Dihoru el at 2017. The scale of the models was mainly determined by the platform size and capacity of the UOB's earthquake simulator, by aspects of design and manufacturing and by the complexity and convenience of installation of the measurement system. The material for the model components (acetal) had to seek a reasonable approximation for the ratio between the scaling factor for density (S_r) and the scaling factor for stiffness (S_E). In addition to that, the selection of the model material was determined by the requirements of rigidity (to allow manufacturing to very tight tolerances and rigid component interactions), non-hygroscopicity (to secure dimensional stability in time) and friction properties comparable to those of the prototype material. Figure 1 shows the arrangement of graphite components in a real core (a, b) and the layout of acetal components in the SLA rig (c, d). While the degree of representation of the model for the aforementioned AGR cores is important, the physical model design was primarily guided by the objectives set out by the computer modellers for the validation work. The model array sits on a stainless steel base within the lateral confinement of a rigid octagonal restraint frame. In order to decrease friction, a layer of 0.5mm diameter glass beads was applied at the interface between the acetal components and the stainless steel base. The decrease of friction was dictated by the requirement that the SLA should model the displacement behaviour of the components in the layers 4-7 of the real core, where sliding friction is not present. The SLA rig is rigidly attached to the platform of the UOB

earthquake simulator (‘shaking table’). Overall, the very simple boundary conditions in the SLA rig make the rig data easier to understand and compare with the outputs of the numerical models. The SLA contains 284 model lattice bricks, 301 model interstitial bricks and 586 model loose bearing keys (Figure 1d) in its intact configuration.

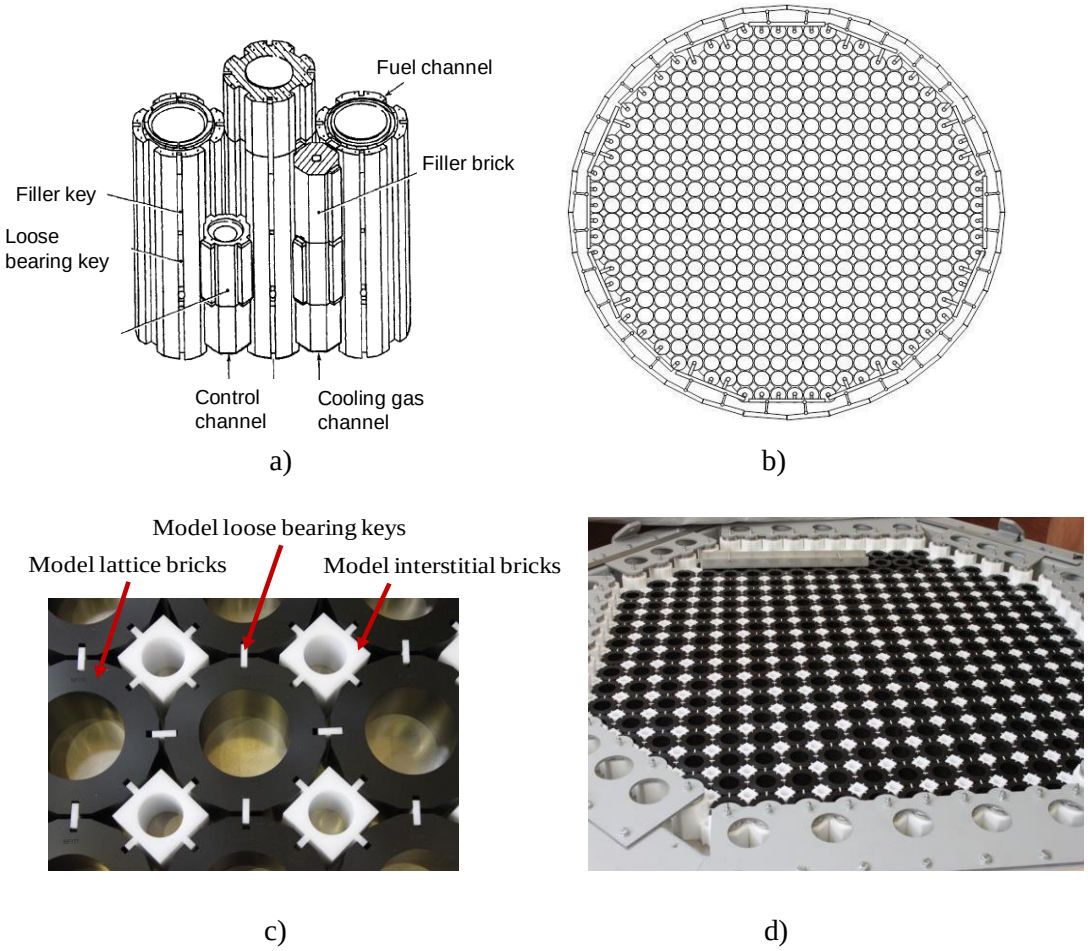

Figure 1 Component layout in an AGR core: a) 3D view, b) plan view. Model component layout in the SLA: c) component arrangement detail, d) overall view of the SLA array.

The intact model lattice bricks can be replaced with up to 142 model doubly cracked lattice bricks (DCBs) (Figure 2c) that can be used in various locations and orientations to simulate a degraded core.

When subject to fast neutron radiation, the graphite undergoes dimensional change which manifests itself as changes in the diameters of the fuel bricks. These changes, which are not uniform along the length of the brick or around the circumference, may lead to cracks. A singly cracked brick (i.e. a brick with one crack along its height) may develop into a doubly-cracked brick (i.e. a brick with two cracks along its height situated at opposite keyway locations). A doubly-cracked brick has the potential to disturb the keying system by the movement (separation or shear) of its two halves and this was the reason why it was considered in modelling.

Given the large number of components keyed together along the cardinal and the 45 degrees directions, the dynamic displacement response is governed by the brick-to-brick and the key-keyway clearances whose non-linear and time-dependant changes are determined by dynamic input, local geometry and component location in the array. When the array is subjected to a dynamic loading, the forces are transmitted via the keying system (Figure 2b), hence the importance of having the keys undamaged and engaged in the keyways. In model arrays containing simulated doubly cracked model lattice bricks (DCBs), the two halves of a cracked brick may separate or shear relative to each other (Figure 2c), affecting the integrity of the keying system by causing loose bearing keys and/or interstitial brick keys (integral keys) to come out of their respective keyways. Due do its designed clearances and component

geometries, the rig presents the potential for key-keyway disengagement which may result in local/overall distortion of the array. In the prototype core, any local distortion may affect the control rod channel and/or the fuel channel shapes. Although the SLA rig only models one single layer of the core and its outputs cannot be directly translatable to full-core numerical models, the SLA response is a good indicator of the way the effect of damage (key disengagement and/or presence of cracked bricks) propagates inside the array. In consequence, monitoring the component movement (including keys and cracked brick halves) in the SLA model becomes significant for understanding the core mechanics.

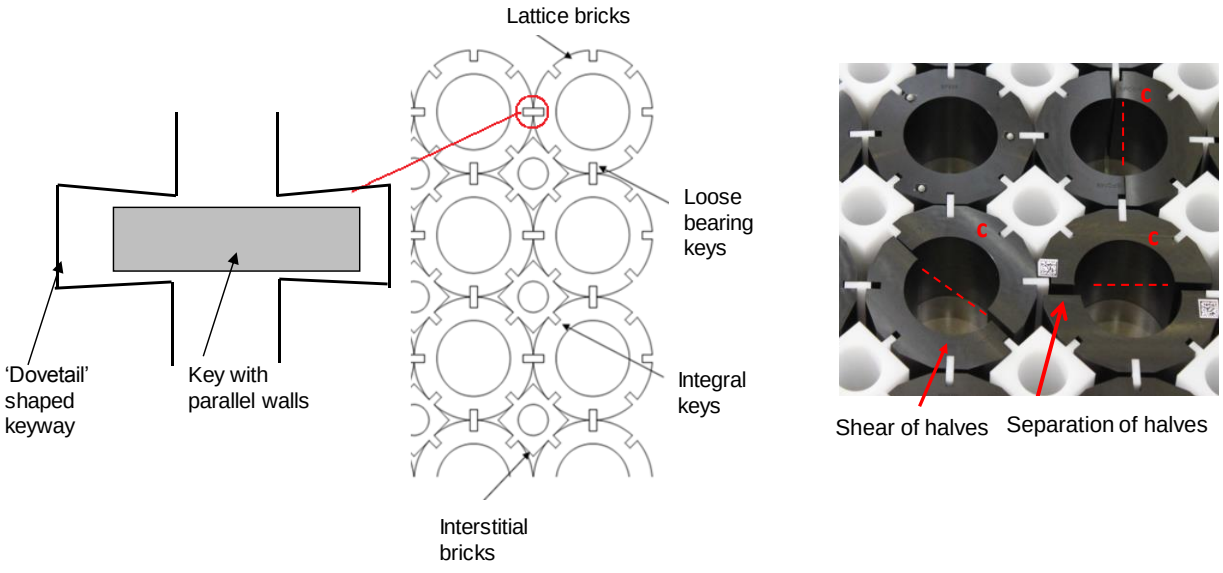

Figure 2 The SLA keying system (a: detail, b: general view) and model cracked bricks embedded in the array (c).

4. Computer Vision Based System Approach

The computer vision based system employed in component tracking consisted of an infrared vision (IRV) system and a high speed video (HSV) system working in synchronization with a conventional data acquisition (DAQ) system (Figure 3). The IRV and the HSV systems dealt with component tracking, while the conventional DAQ was used to collect the accelerometer data. The common clock generator supplied clock signals at frequencies of 5000Hz for the DAQ, divided down to 100Hz for the IRV and 50Hz for the HSV.

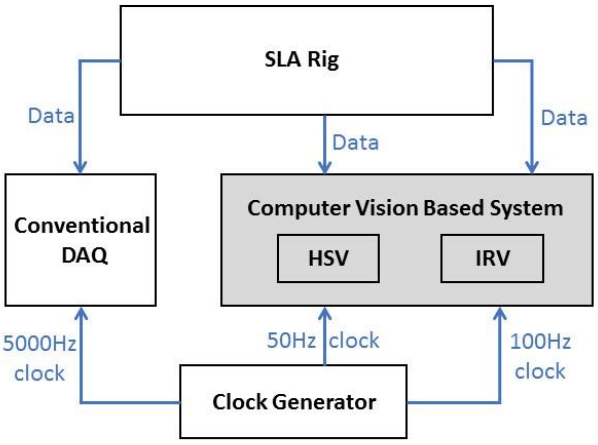

Figure 3 Diagram of SLA systems.

4.1 The IRV System: Architecture And Mode Of Operation

Five Oqus400 cameras (from Qualisys AB) were employed in infrared mode to track the passive markers attached to selected array components (Figure 4). The Oqus400 sensors (sensor size: 13.568mm x 13.680mm, pixel size:8µm) work with modulated light with a frequency of 33 kHz and wavelengths between 800nm and 1100nm ('near infrared'). The passive markers are almost spherical or hemispherical parts covered with special paint that reflects the radiation in that particular wavelength range (Figure 4a).

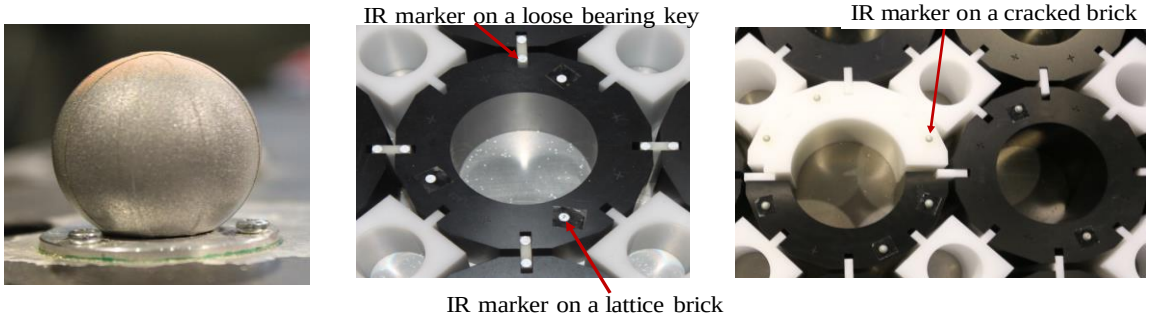

Figure 4 a) IR passive marker (detail photo), b) IR markers attached to loose bearing keys and lattice bricks, c) IR markers attached to cracked bricks.

A theoretical investigation was carried out in order to select the lenses to suit the performance requirements of the measurement and to design the rigid scaffolding structure to hold the cameras at optimum distances above the model array which sits on the shaking table platform. The distance between the camera and the array surface (Figure 5) determines the measurement accuracy and resolution, the design of the camera support system and the convenience of camera adjustment and operation. The size of the object (overall footprint ~3m x 3m) determines the required field of view (FOW) and the minimum focal distance (D), which, in practical terms determines the elevation of the camera above the shaking table (Z). A selection of candidate lenses were considered for this application. Based on the minimum focal distance for the required coverage in the horizontal plane and assuming that the optical axis of the camera passes through the centre of the shaking table, the required elevation of the camera above the array, Z, was calculated (Figure 5b).

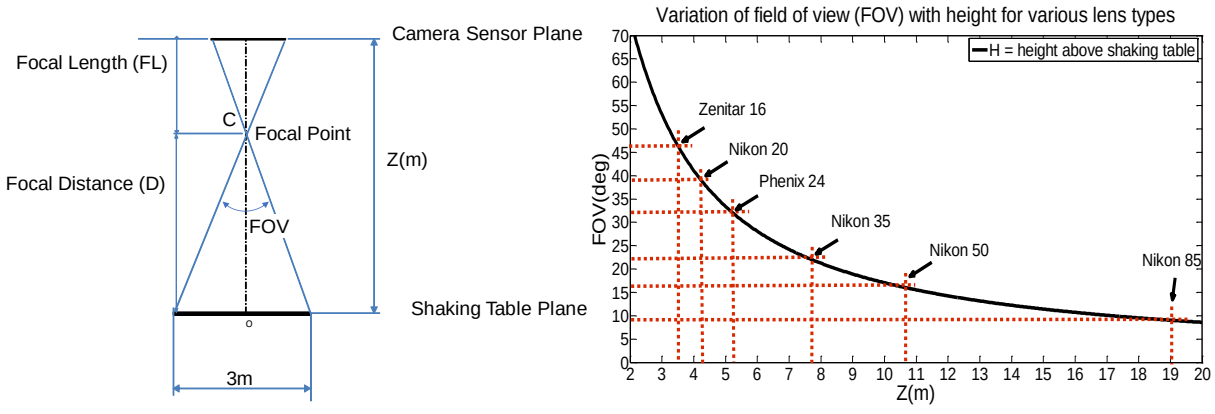

Figure 5 Geometrical layout with IR camera above the shaking table (a:generic optical characteristics). Required elevation (Z) of camera above the shaking table for various lens types (b).

The Zenitar 16 (a wide angle lens that caters for large fields of view) was selected to work with the Oqus400 cameras, at an elevation (Z) of 3.5m above the shaking table (Figure 5b). As with any typical wide angle lens, the images can be affected by barrel distortion (Figure 6), i.e. the image magnification decreases with distance from the optical axis. A linearization software (QTM from Qualisys AB) was applied to remap the curvilinear images produced by the fish-eye lens to a conventional rectilinear projection. The correction was applied to both IR marker data as well as video data displayed in QTM in order for the video overlay to be corrected.

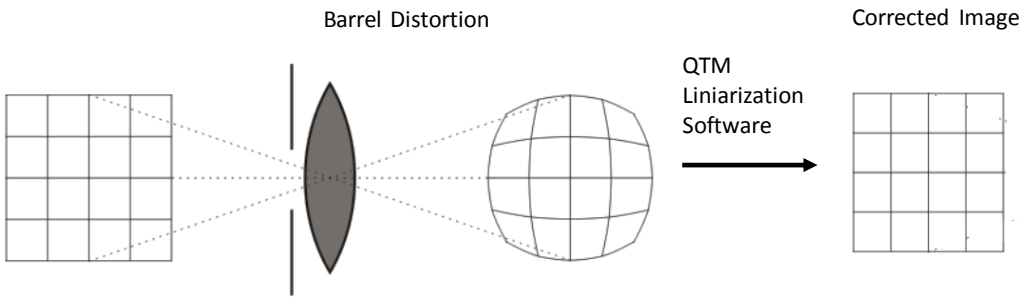

Figure 6 Application of QTM linearization software to correct image barrel distortion.

After the required distance between the cameras and the SLA rig was established, a rigid aluminium scaffolding system was built around the shaking table to host the IRV and the HSV systems (Figure 7). Before each session of testing, the IRV system was subjected to a calibration procedure that defined the distances between the IR markers and the volume in which the camera system would operate in the shaking table system of reference. A snaphot taken during the calibration procedure is shown in Figure 8. Calibration markers were installed at precisely known positions around the array in order to define the calibration factor for length for a given geometrical layout of the cameras.

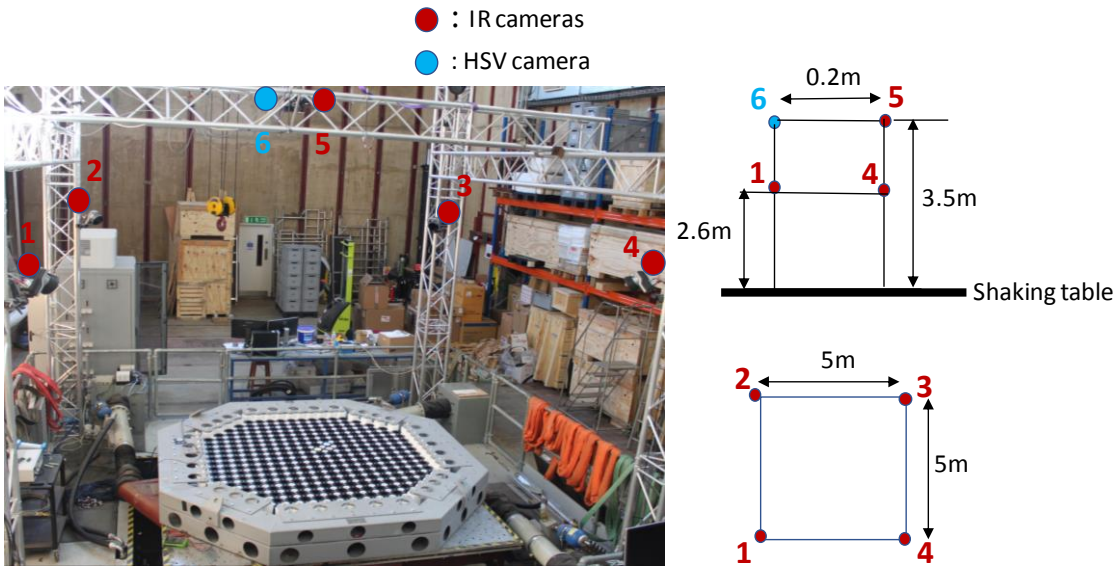

Figure 7 IR (nos. 1-5) and HSV (no. 6) cameras installed on a bespoke scaffolding system, overlooking the SLA.

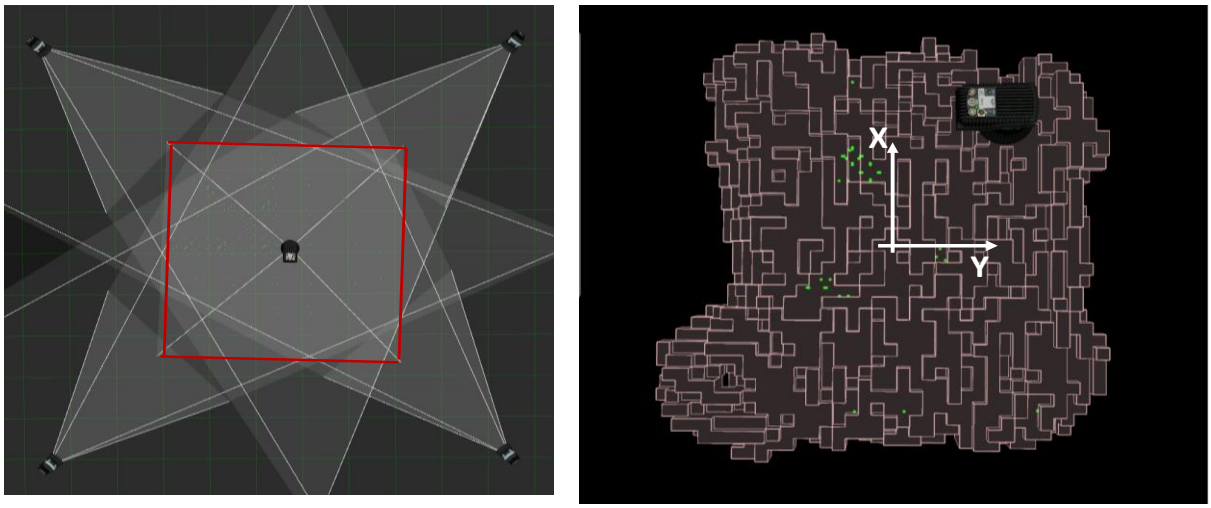

a) b)

Figure 8 Camera cones of view and shaking table plaform (red frame) (a) and snapshot of calibration volume in infrared mode, showing IR markers (green dots) and the shaking table reference system (white axes) (b).

4.2 The HSV System: Architecture And Mode Of Operation

The HSV system consisted of a 4096pixel x 3072pixel (12.6Mpixel) high-speed camera, type Teledyne Dalsa Falcon 12M, that captures images at a speed of 50 frames per second (fps). The acquisition frequency of the camera was considered suitable for capturing component displacement in the seismic studies as the seismic inputs employed in tests had a typical frequency band of 0-20Hz, with the most significant energy band around 2-5 Hz.The camera was located above the array, in central position as shown in Figure 7. Four LED lights, type Chauvet C5876314S Colorado Zoom WW Tour LED, were attached to the four corners of the camera support frame in order to provide a stable light source. The HSV camera was operated in external trigger mode, with the clock signal provided by the common clock system of the SLA rig. The video records were delivered in *.avi* format. The calibration of the HSV images was carried out in LabVIEW (a development platform for graphical programming from National Instruments Inc.). Figure 9 shows a snaphot of video image calibration, showing selected points situated at known relative distances between one another in the rig. By measuring the distances between a large number of selected points (min. 20) in the image, an average calibration factor of 0.78mm/pixel was statistically calculated.

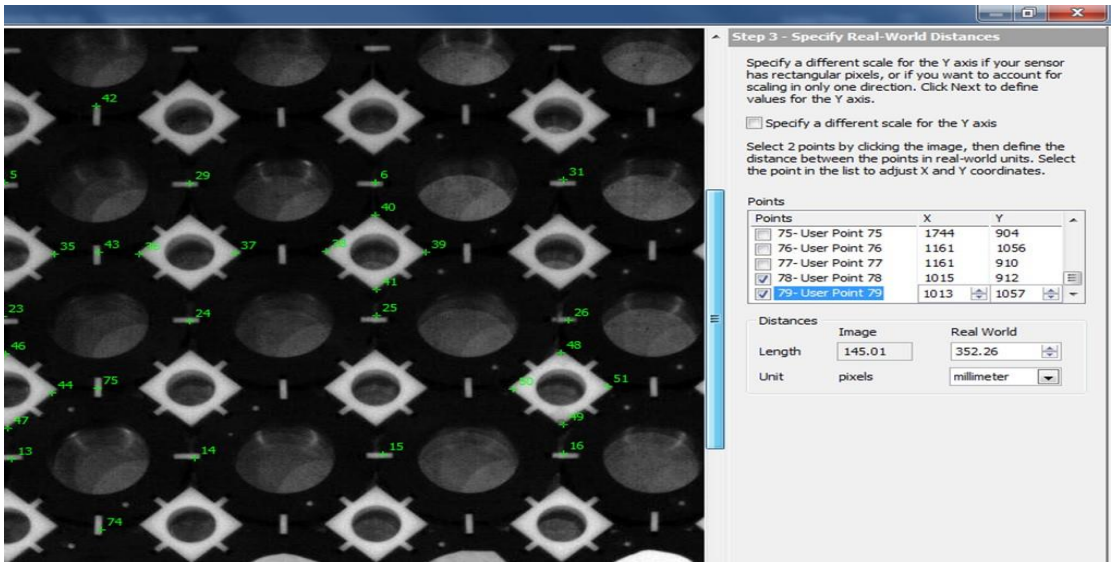

Figure 9 An image extracted from an *.avi* record undergoing the calibration procedure. The points shown in green were selected to define the scaling factor for length.

4.3. Dynamic Tracking

4.3.1 Dynamic Tracking via IRV System

The IRV data capture was performed by the Qualisys Track Manager (QTM) software associated with the Oqus system. Data capture was triggered by the external clock. Data were exported automatically in Matlab format. The initial analysis consisted of linear transformations of the spatial coordinate data and was undertaken in Matlab with minimal coding. The relative movements of the array components were inferred by subtracting the component marker coordinates from the restraint / template marker coordinates. Further, more advanced, data processing for displacement mapping across the array was carried out also in Matlab .

4.3.2 Dynamic Tracking via the HSV System

A bespoke high-speed video processing code was developed in LabVIEW for the following tasks:

i) Image calibration
ii) Pattern recognition
iii) Object tracking

The code reads the video records frame by frame and applies the 'mm-per-pixel' conversion factor to each 8-bit greyscale image. A pattern recognition algorithm is applied to the image so that all objects that have common features (grey level intensity, geometry, size, orientation, etc) are identified. The identified objects are then tracked based on the Lucas Kanade optical flow (LKOF) computation (Lucas & Kanade 1981, Rojas 2010). The LKOF algorithm provides an estimate of the displacement of selected objects in successive images of a scene. In this application, the centre of symmetry of a selected array component (i.e. loose bearing key, lattice brick, interstitial brick or cracked brick half) was tracked and its position vector in the horizontal plane was given as an output for each recorded frame of the HSV record.

4.3.2.1 Object Identification

Physical templates of bricks, keys and brick halves were rigidly attached to the SLA rig frame to serve as references in object identification.The video records contain 8-bit grayscale images of the array that consists in an assembly of objects following a repetitive pattern. The first task was to recognize these objects and identify (label) them. For this purpose, a template image of the object to be matched was correlated across the image and the correlation value used to determine the best match. The pattern matching is based on a greyscale value pyramid matching: the top-level (level 0) of the image in the search pyramid is correlated with the top-level (level 0) of the template. This results in a number of likely matches. For each of these likely matches, the same search procedure is then performed at each level of the pyramid (level 1, level 2, or deeper levels) (Figure 10a), in order to find the best possible match. Image cross-correlation is similar to cross-corelation in signal processing and produces the integral of the pointwise multiplication of the original functions (the greylevel pixel intensity in image and template in this case), in order to quantify the difference between the two. The pattern recognition algorithm also contains several other object matching citeria that complement the greyscale value function matching, i.e. number of expected matches, minimum separation between matches, maximum match overlap, number of subpixel iterations, number of rotated patterns and maximum angle of patterns rotation. For this application, a search pyramid with 3 levels and 20 subpixel iterations was employed. An example of cross-corelation between template and array image is shown in Figure 10b.

Figures 11 and 12 show the identification of objects (loose bearing keys, interstitial bricks, lattice bricks and cracked brick halves) in the SLA.

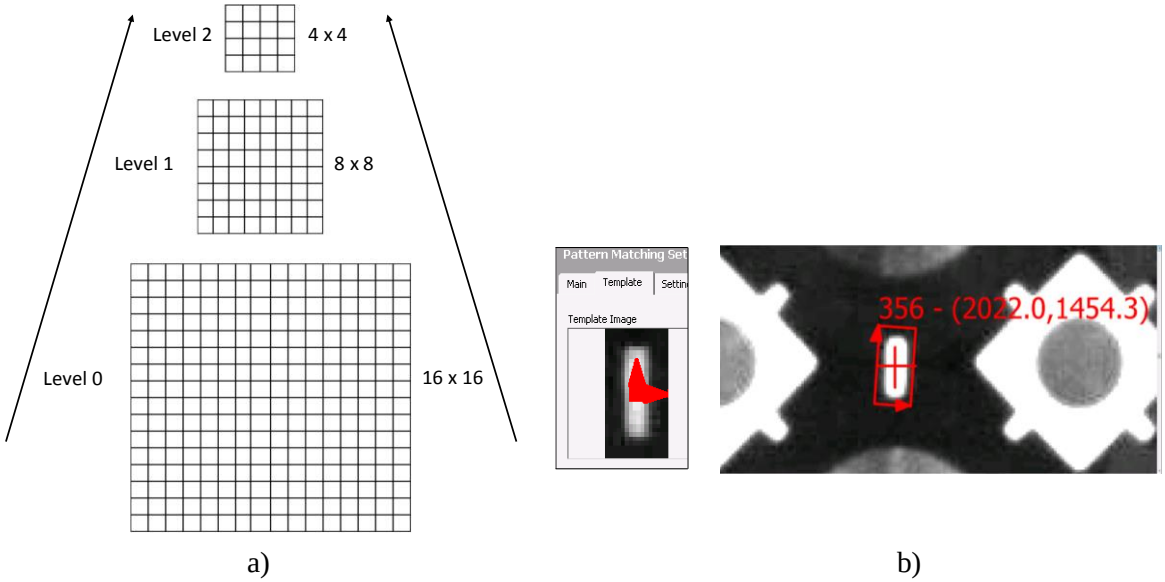

a) b)

Figure 10 Diagram showing the search procedure in greyscale value pyramid matching (a) and template for loose bearing key matched against the greyscale image of the array (b)

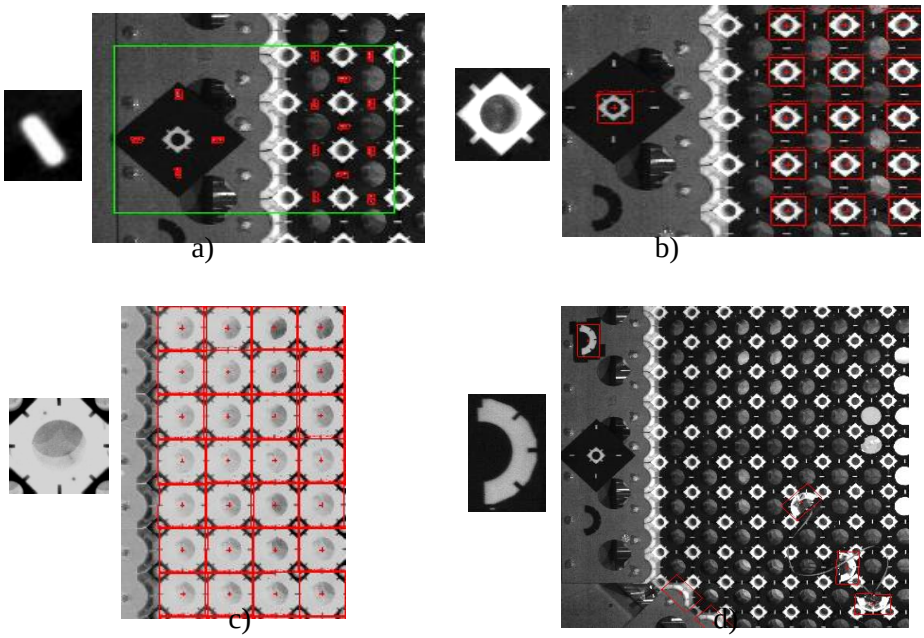

a) b) c) d)

Figure 11 Identified components (marked in red window) and the templates employed in pattern recognition (shown on the left of each frame) (a: loose bearing keys, b: interstitial bricks, c: lattice bricks (after image inversion), d: white cracked brick halves). The pattern recognition algorithm compares the templates with the objects in the frames.

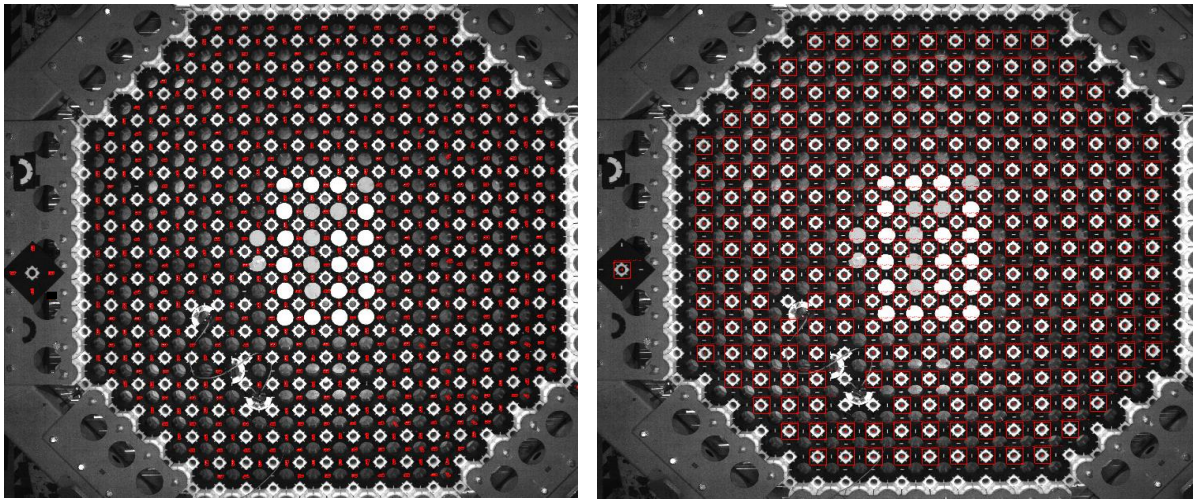

a) b)

Figure 12 LabVIEW video processing window showing the identification (in red) of all the loose bearing keys (a) and all the interstitial bricks in the array (b). The identified keys are shown as red objects (a) and the identified bricks are shown in red frames (b)

4.3.2.2 Optical Flow Based Tracking Algorithm

After the identification (labelling) of objects, the code performs the object tracking in successive image frames via optical flow. Optical flow has been used used extensively by researchers in many areas such as object detection and tracking, movement detection, robot navigation and visual odometry (Kelson et al 2008). The optical flow principle can be explained by a simple scene viewed through a square hole as in Figure 13. If we view a pixel of 2D coordinates *(x, y)* through the square hole, its brightness (intensity) will change from frame '*n'* to frame '*n+1'*. The change in brightness between the two successive frames is assumed to have been caused by a small displacement of pixel *(x,y)* under observation. As the brightness has increased from frame '*n*' to frame '*n+1'*, it is fair to say that the *(x, y)* pixel has moved towards the left and upwards, as shown in the diagram.

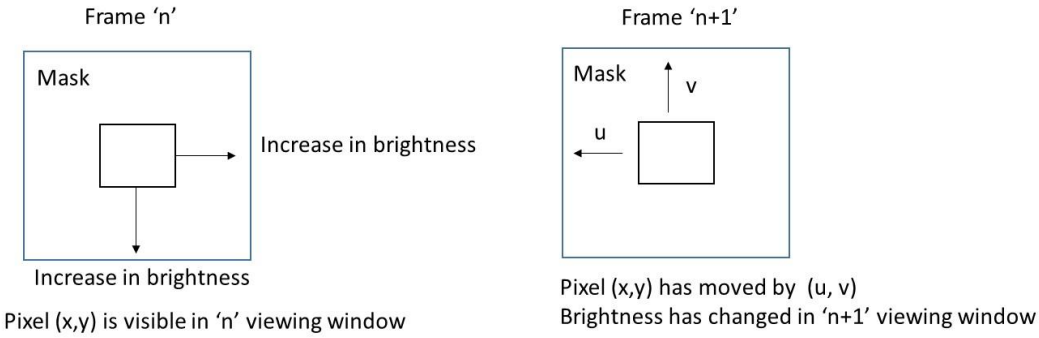

Figure 13 Simple square hole scene explaining the optical flow principle.

If the increase in brightness per pixel at pixel *(x,y)* is $I_x(x,y)$ in the *x* -direction and $I_y(x,y)$ in the *y* -direction, then the total change in brightness after a movement with velocity *u* in the *x* -direction and velocity *v* in the *y* -direction would need to match the local difference of brightness in the square window, $I_t(x,y)$ (Equation 1).

$$Ix(x,y) * u + Iy(x,y) * v = -It(x,y) \quad (1)$$

As a single pixel is too small a 'structure' for brightness matching, the optical flow equations are applied, in practice, to a 'window' of pixels that defines the neighbourhood of a certain pixel *(x,y).* For

example, if the neighbourhood window around *(x,y)* is 3x3 pixels, then 9 optical flow equations (Equations 2-4) can be written.

$$Ix(x1, y1) * u + Iy(x1, y1) * v = -It(x1, y1) \quad (2)$$
$$Ix(x2, y2) * u + Iy(x2, y2) * v = -It(x2, y2) \quad (3)$$

⋮

$$Ix(x9, y9) * u + Iy(x9, y9) * v = -It(x9, y9) \quad (4)$$

where *Ix,Iy,It* are the partial derivatives of brightness with respect to position *x*, *y* and time *t*, and *(u,v)* is the local optical flow (velocity vector).
Equations 2-4 can be written in matrix form:

$$A * V = B \quad (5)$$

where

$$A = \begin{pmatrix} Ix(x1, y1) & Iy(x1, y1) \\ Ix(x2, y2) & Iy(x2, y2) \\ \vdots & \vdots \\ Ix(x9, y9) & Iy(x9, y9) \end{pmatrix}, \quad V = \begin{pmatrix} u \\ v \end{pmatrix}, \quad B = \begin{pmatrix} -It(x1, y1 \\ -It(x2, y2 \\ \vdots \\ -It(x9, y9) \end{pmatrix} \quad (6)$$

By multiplying by A^T (the transpose matrix of *A*), Equation 5 can be rewritten as:

$$A^T * A * V = A^T * B \quad (7)$$

$$V = (A^T A)^{-1} A^T B \quad (8)$$

The system of equations (8) shown above shows that the velocity vector associated with a certain window of pixels could be inferred from computing the spatial and temporal variations of brightness in that window. It is obvious that the above system has more equations than unknowns, thus it is over-determined. The LKOF method proposes an estimate for the optical flow based on a least squares approximation, assuming that the movement between the two successive frames is very small, so that the differential equation of optical flow (Equation 1) holds. For the SLA project, the LKOF algorithm was implemented in the Vision Assistant module of LabVIEW. A window setting of 3 pixel x 3 pixel was employed.

4.3.2.3 HSV Output Files

For a typical seismic test lasting ~15s and for an image size of ~12Mpixel, taken at a frame rate of 50 frames per second, the resulting video output file is ~700 Mb. The HSV processing including image calibration, pattern recognition and object tracking takes between 20-30 min, with shorter times for lattice brick tracking (number of objects: 284) and longer times for loose bearing keys (number of objects: 586). The HSV processed data output files consist of *.txt* files showing the frame number, the component's identification number, the *x* and *y* coordinates (in 'mm') of its centre of symmetry, the orientation angle and the degree of matching the template (score) (Table 2). The *x-y-z* system of coordinates is the reference system set up in the calibration stage. The *x* and y axes are aligned with the Qualisys calibration frame and the *z* axis is oriented upwards, perpendicular to the array plane. The relative displacement time histories of the array components are obtained by subtracting the restraint displacement time history from the absolute displacement time history of the component.

Table 2 Example of video processing output *.txt* file (shown for 10 tracked interstitial bricks)

Object #	X Position (mm)	Y Position (mm)	Angle (deg)	Score
1	1597.64661	2159.95313	0.12772	951.4377
2	2162.96631	2717.89453	357.44971	950.2913
3	1597.13611	2018.6582	0.44517	949.4247
4	1740.04944	2715.47388	357.21036	947.8153
5	1881.12854	2718.59253	358.04807	945.1423
6	2727.37964	2438.02393	358.09824	943.9703
7	1738.21399	2018.18945	359.7764	942.9056
8	2303.6084	2716.3894	357.8222	942.1597
9	1457.41699	2436.57544	356.85464	941.9182
10	2022.22302	2439.00928	0.01512	940.9347

4.3.2.4 Tracking Performance

a) Resolution & Noise Level

The video records contain images in which the pixel size is ~0.78mm (dictated by the sensor of the HSV camera). The LKOF tracking algorithm performs image brightness computations between pixels, hence the instant location of the centre of symmetry of a component is calculated at subpixel accuracy. The X and Y coordinates of the centre of symmetry is reported down to micron level (see Table 2). However, the noise level in the measurements is ultimately the threshold parameter that limits the resolution. Figure 14 shows the first part of the time history from records of displacement relative to the rig frame for two keys (one situated near the array centre (K321) and one situated near the array boundary (K393), before the shaking table started moving. Hence, the plots illustrate the noise recorded when the array was stationary. The noise level stayed in the same (-0.1-0.1) mm range for both keys, in both tests. This suggests that the tracking algorithm works in a similar fashion across the array and that, in spite of the large area of the array, the combined noise level (optical and computational) stays in the same (-0.1-0.1) mm range.

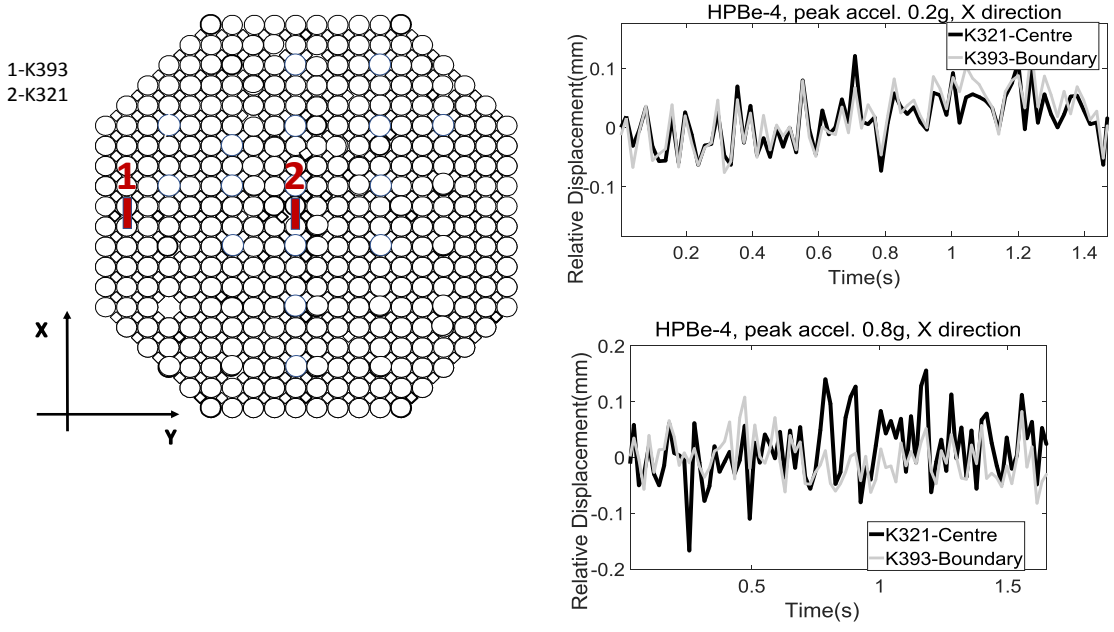

Figure 14 Noise level recorded in two seismic tests of different amplitude (peak acceleration: 0.2g and 0.8g, HPBe-4: seismic input) for displacement relative to rig frame measured for keys K393 (near boundary) and K321 (near centre).

b) Comparison Between HSV and IRV Measurements

A comparison between the HSV and the IR measurements of relative displacement for keys K1914 and K1912 (Figure 15) is shown in Figure 16. It is important to note that the comparison is not like-for-

like, as the HSV system tracks the location of the centre of symmetry, while the IR system tracks the IR markers that are situated at the extremities of the key (see instrumented key in Figure 15). The comparison shows that the IR and the HSV traces follow patterns within 1mm of each other.

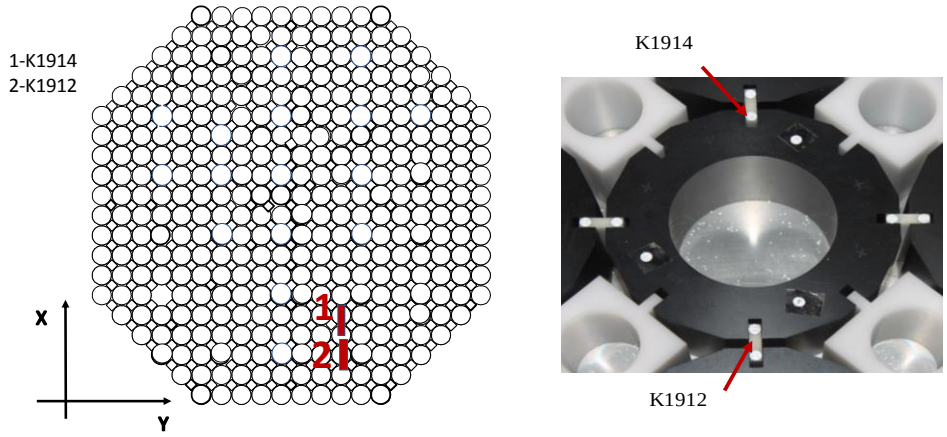

Figure 15 Location of loose bearing keys K1914 and K1912 equipped with IR markers.

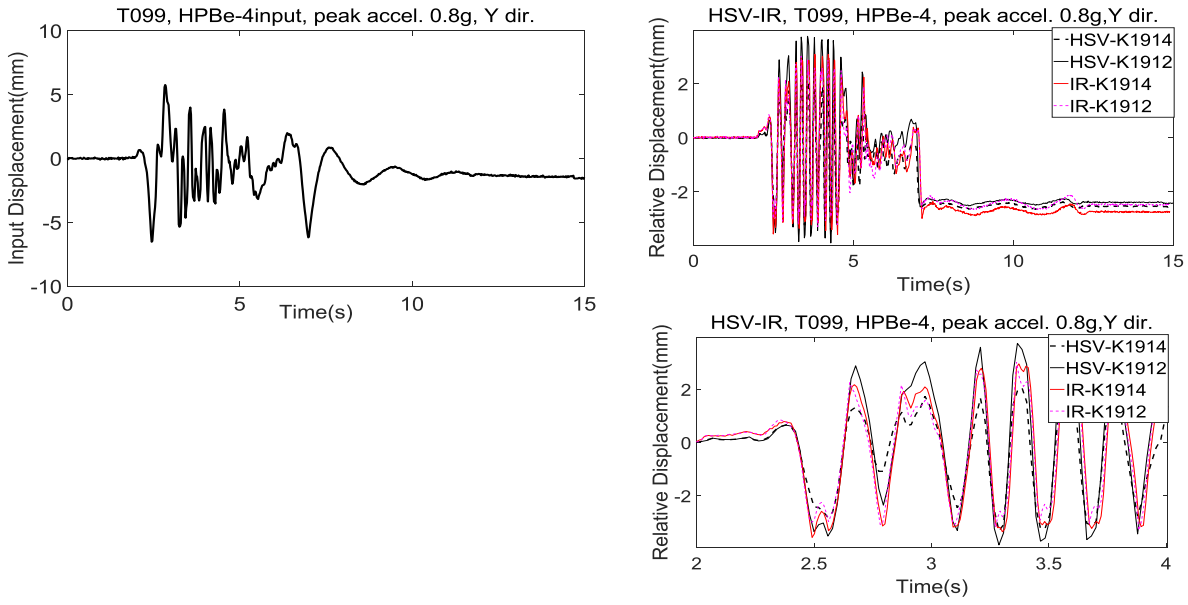

a) b)

Figure 16 Input displacement (a) and relative displacement of keys K1914and K1912 measured via IR and via HSV (b: top: entire time history, bottom:detail).

c) Errors

c1) Image quality errors

Image quality can affect the object tracking precision and accuracy. Out-of-focus and blurry objects with indistinct edges present grayscale histograms that are difficult to interpret in the tracking software. Mitigation: The aperture and the focus on the camera are set up suitably to produce an image that is sharp and bright and with adequate contrast between the black and the white objects.

c2) Image calibration errors

Image calibration involves setting up reference pointers on objects whose physical dimensions are known (Figure 9). The subjectivity of the operator may affect this process. The uncertainty of pointer

location on the image may lead to accuracy errors in the evaluation of the calibration factor (the 'pixel-to-mm' conversion factor).
Mitigation:Employ a large number of pointers on several types of objects for which the real physical dimensions are known. Refer to pointers that are close to one another, but also to pointers that are far from one another. The final calibration factor is computed statistically from a sufficiently rich set of image measurements.

c3) Optical flow errors
This refers to errors caused by the tracking algorithm. The LKOF algorithm computes the spatial and the temporal variations of brightness for each window of pixels (3x3 pixels) in the image. A template image of the object to be matched is correlated across the image and the correlation value used to determine the best match. If the object's margins are not distinct enough, errors of interpretation may affect the computation of the centre of mass location.
Mitigation: In order to enhance the cross-correlation, several additional object matching criteria are employed, i.e. number of expected matches, minimum separation between matches, maximum match overlap, number of subpixel iterations, number of rotated patterns and maximum angle of patterns rotation.

5. Tracking Results and Application to Model AGR Core Behaviour

Without attempting to characterize the dynamic response of the core array in detail, this section shows how the the computer vision based system yields maps of maximum displacement response and statistical displacement maps that can help with evaluating the seismic resilience of the core. Such maps reveal areas of the core that are more prone to distortion (with implications for control and fuel channel shapes) and component locations and orientations that are associated with a higher risk of key-keyway disengagement. A summary of tracking results is presented here with applicability to model core dynamic behaviour.

a) Effect of input amplitude and component location on response
Two keys situated in different locations in the array (near the centre (K321) and near the boundary (K321), as in Figure 17) have been selected to show the effect of input amplitude and key location on displacement response. The selected keys are oriented on X direction (i.e. they are parallel to the input orientation). Figure 17 shows the displacement relative to the restraint frame for the selected keys. The response is given for two tests with different input amplitudes (T001, HPBe-4 input, peak acceleration: 0.2g and T007, HPBe-4 input, peak acceleration: 0.8g). Both tests were run on X direction. As the SLA restraint frame is rigidly attached to the shaking table platform, the restraint input is similar to the applied seismic input. The response displacement magnitude increases with input amplitude and the keys situated near the centre are more mobile than those near the boundary. The keys situated near the centre have larger remnant displacement, as the mobility of the array is larger in the centre and the probability of a key being situated further from its initial position at the end of the test is higher. The increased mobility at the centre can be associated with an increased risk of key-keyway disengagement.This finding is applicable to the prototype core behaviour, i.e. the channels situated near the centre of the core are more prone to distortion.

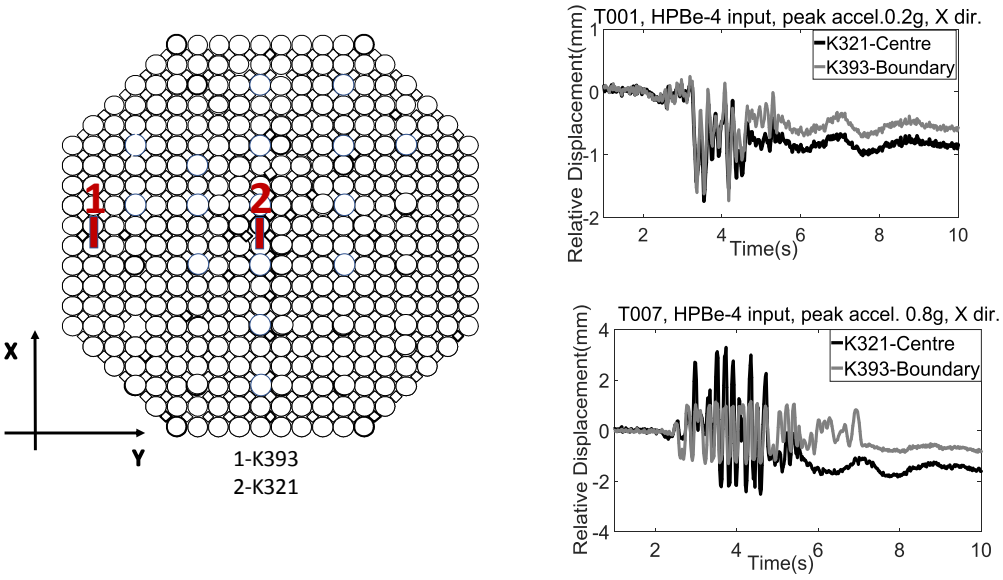

Figure 17 Effect of input amplitude and key location on response (seismic input in the X direction).

b)Effect of input amplitude and input orientation on maximum response

Figure 18 shows the maximum relative displacement in the X direction (a) and the maximum relative displacement in the Y direction (b) , recorded in tests run at different amplitudes (peak acceleration levels: 0.2g, 0.4g and 0.8g), with input applied on three different orientations (X, 45deg and Y). The relative displacement on X is largest for tests run on X direction and for tests run at higher amplitude. The relative displacement on Y is largest for in tests run on Y direction and for tests run at higher amplitude. As expected, the smallest response on Y direction occurs in the tests in which the input is applied on X.

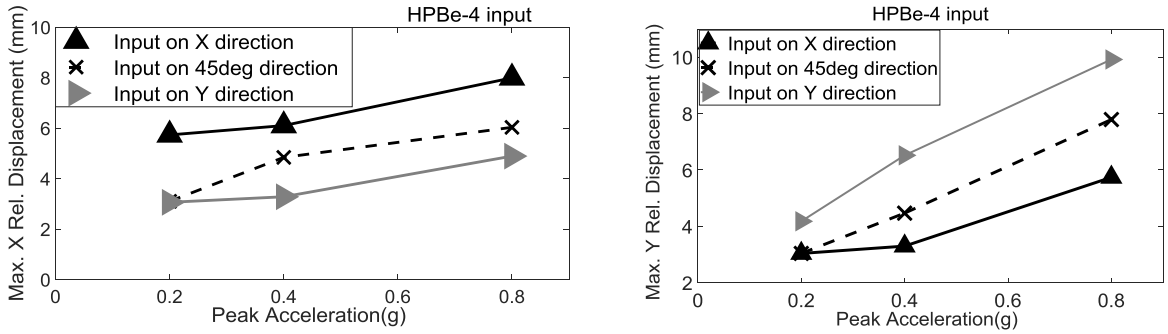

a) b)

Figure 18 Maximum relative displacement of keys on X direction (a) and on Y direction (b), recorded in seismic tests tests for one seismic input run at three peak acceleration levels and three orientations of input (X, Y and 45deg).

Figure 19 shows maximum relative displacement maps for the interstitial bricks across the array, in tests run at three different peak acceleration levels (0.05g, 0.4g and 0.7 g), for two orientations of input (X and Y). Again, the array shows larger relative movements in the central area, showing a slight elongation of maximum response area in the direction of input. These trends are obvious for the larger amplitude shakes (peak acceleration levels of 0.4g and 0.7 g) and not for the low amplitude shake (peak acceleration levels of 0.05g). In the latter, the relative displacement measurements are very small (0.15-0.4mm) and the noise is 'masking' the real displacement response (the signal-to-noise ratio is small).

As in the real core the interstitial bricks form the control rod channels, the maps below are useful in understanding the potenstial for array distortion for certain input magnitude levels and orientations.

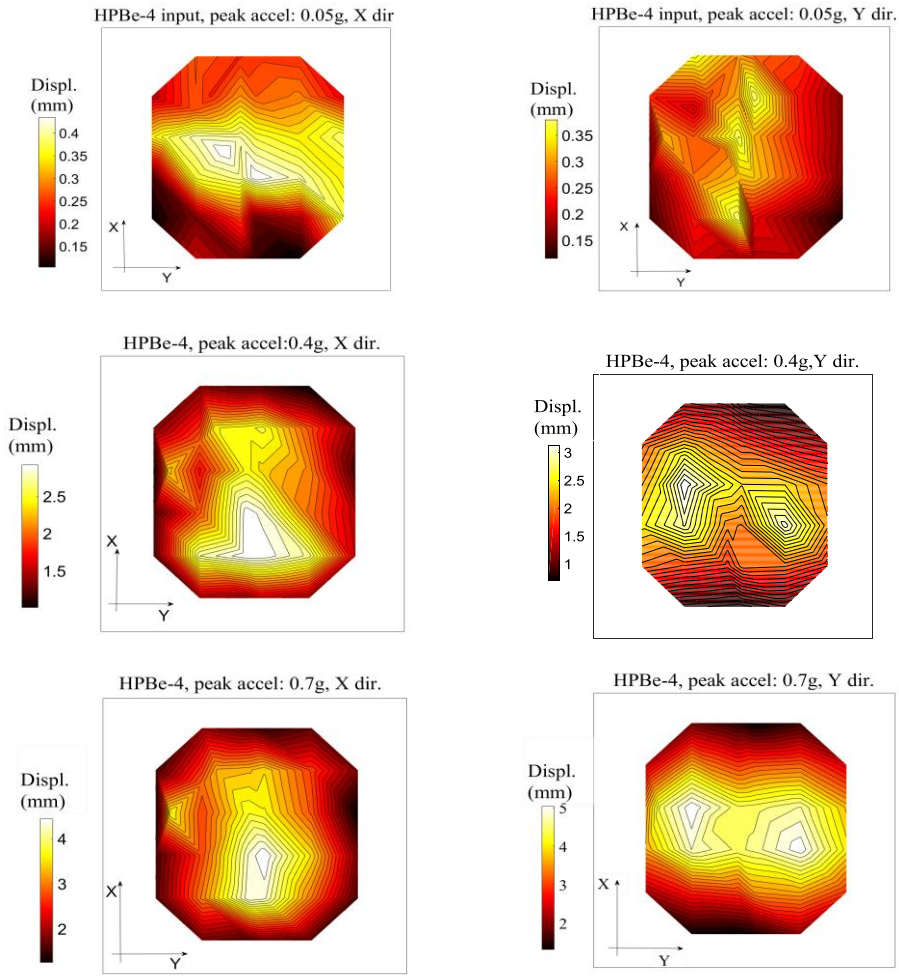

Figure 19 Contours of maximum relative displacement of interstitial bricks recorded in seismic tests, for three peak acceleration levels and two orientations of input (X and Y).

c)Effect of input shape and component location on response

Figure 20 shows the relative displacement traces of two keys located in two different locations (i.e. near the centre and near the boundary, respectively), in three tests run on X direction, in which the input signal's shape was different (T001: seismic, T016: sinusoidal, T031: sinusoidal pulse). As expected, in all three tests, the key response follows the shape of the input signal. There are two paths of seismic input propagation, i.e. via the rig base and via the rig boundary (the circular steel frame surrounding the array). As the input propagates from the boundary towards the centre of the array, the keys in the centre respond later than the keys near the boundary. This delay appears obvious in the pulse test plot. Also, as the array is more lively in the centre, at the end of the tests, the keys situated near the centre are further away from their initial position, compared to the keys near the boundary.

d) Effect of key orientation with respect to input direction

Figure 21 shows the relative displacement traces for four sets of keys (two sets situated near the boundary and two sets situated near the centre). Each set of keys include a key parallel to the input direction and one key perpendicular to the input direction. The traces are recorded in test T009, HPBe-4 input, 160% gain, peak acceleration: 0.8g, Y direction. The keys that are parallel to the input direction display larger relative displacements than those who are perpendicular to the input direction which are in shear, resisting the motion. As they have bigger movements, the parallel keys end up at the end of the test further away from their initial position, compared to the transversal keys. This suggests that the

keys that are parallel to the input direction are at a higher risk of disengagement than the transversal keys.

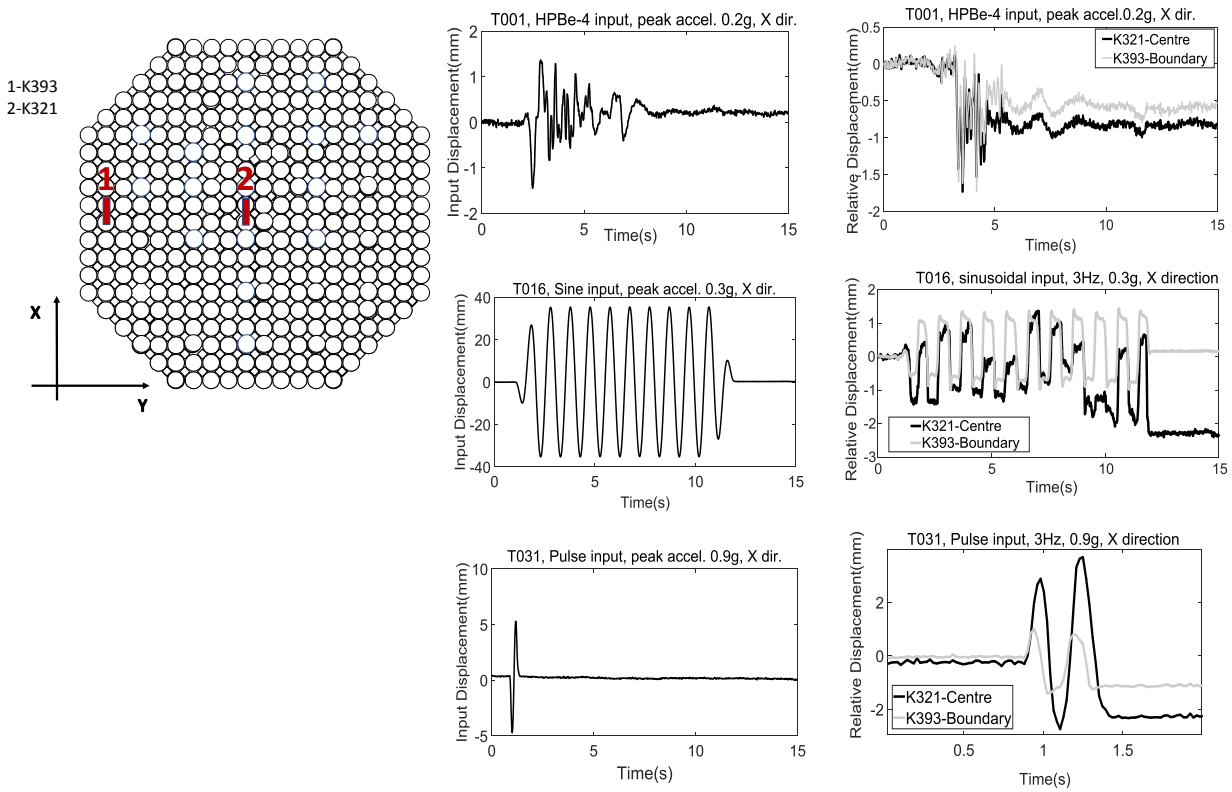

Figure 20 Effect of input shape and key location on keys' relative displacement.

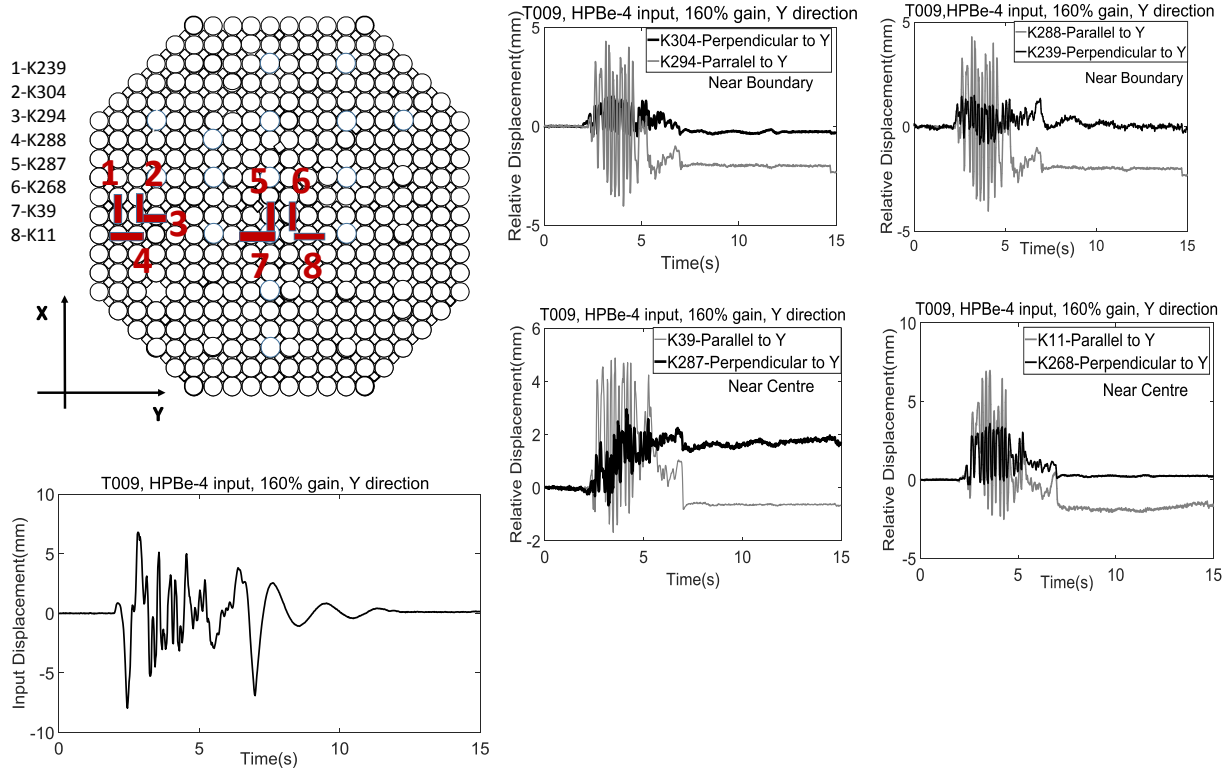

Figure 21 Effect of key orientation with respect to input (note: 160% gain corresponds to 0.8g peak acceleration).

e) Key-keyway disengagement

The tracking data are instrumental in revealing the occurrence of key-keyway disengagement, as exemplified in Figure 22. Two loose bearing keys (K1 and K2) and their adjacent cracked brick half (B1) are tracked in two successive tests (T096 and T098) in which the same seismic input was applied (HPBe-4 input, peak acceleration 0.8g, applied on X direction). While in T096 the keys appear engaged with the cracked brick (Figure 21b), in test T098 the key K1 disengages as shown in the displacement time history shown in Figure 22c. The photo taken at the end of test T098 (Figure 22a) confirms the finding extracted from the measurement data. It is interesting to note that disengagement occurs for the key (K1) parallel with the input direction and not for the key perpendicular to the input (K2), confirming the observations made earlier in point d).

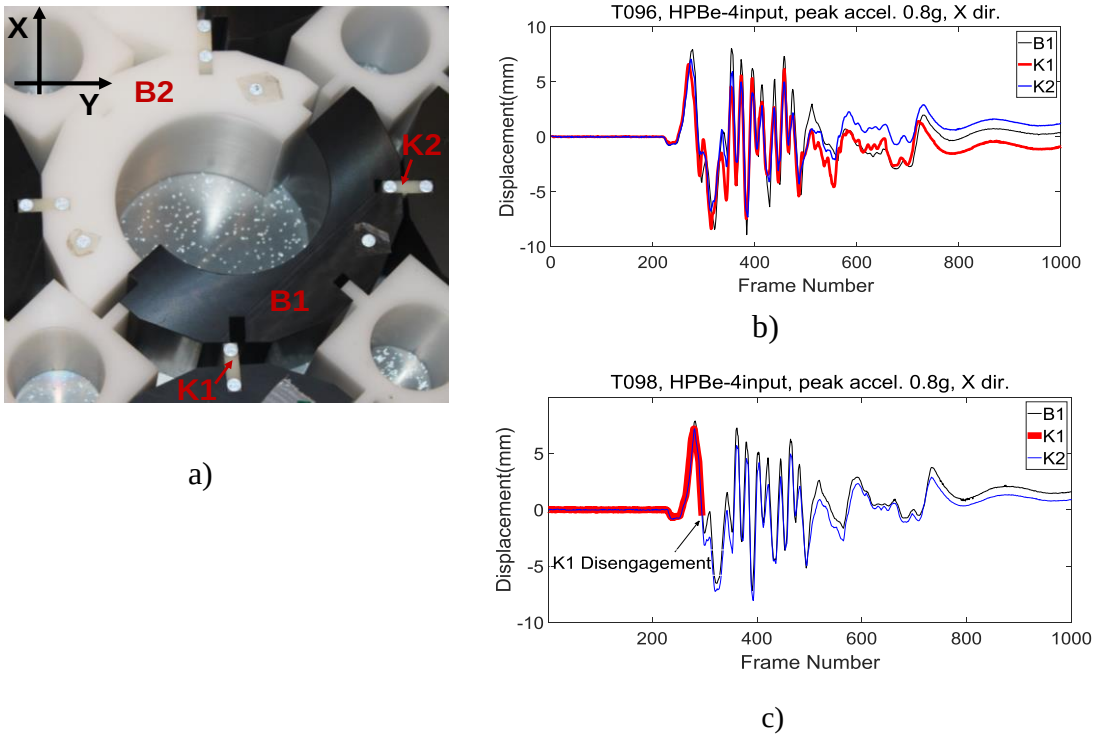

a)

b)

c)

Figure 22 Key disengagement: photo taken at the end of test T098 (a) and displacement time histories of keys K1, K2 and brick half B1, in test T096 (b) and test T098 (c).

f)Histograms of relative displacement bands

Given the large number of components and interactions present in the SLA rig, the understanding of its dynamics has to be supported by statistical tools that could reveal trends and patterns useful for behaviour interpretation. An example is shown in Figure 23, where histograms of key relative displacement are presented for seismic tests of different input amplitude and input orientation. The histograms show displacement bands and the number of keys associated with those bands. This representation can be useful in assessing the evolution of disengagement risk for certain dynamic inputs. In this particular example, it can be noted that the X relative displacement increases with input amplitude and that the X displacement is largest in tests when the input is parallel to X and smallest for tests run on Y direction. Similar maps can be represented for model interstitial and lattice bricks.

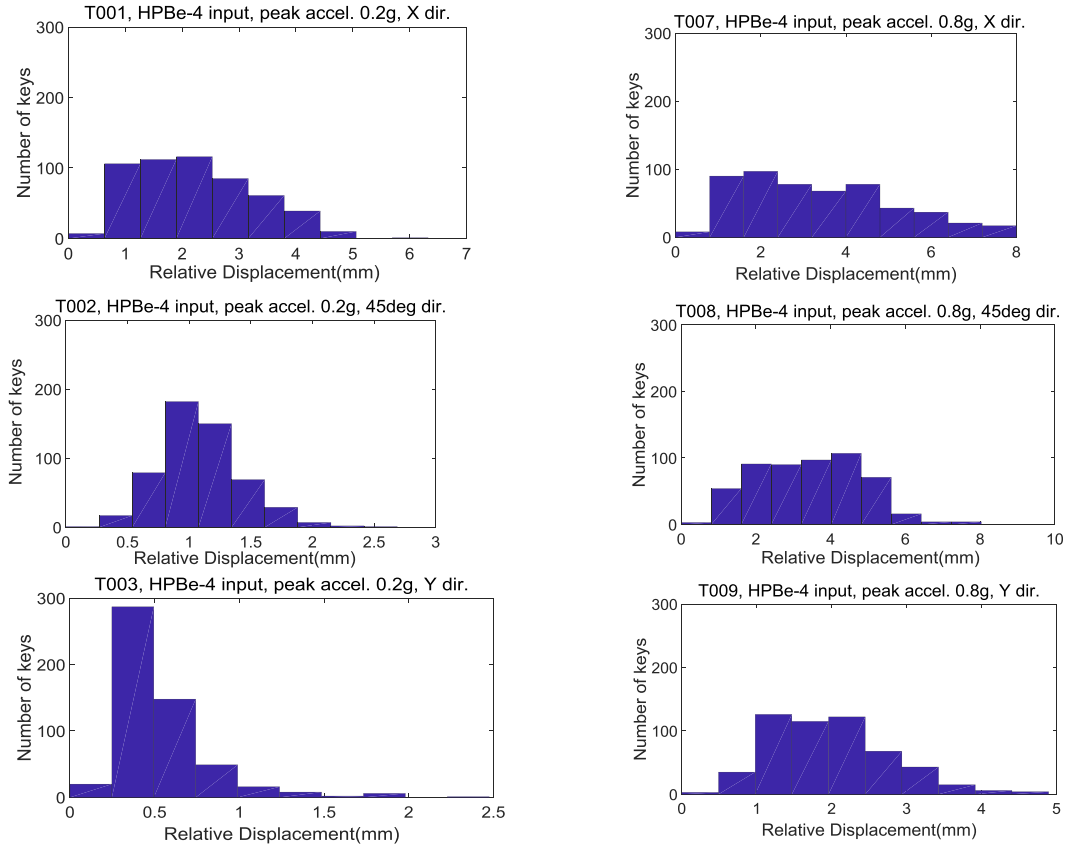

Figure 23 Histograms showing relative displacement in the X direction in different seismic tests.

6. Concluding Remarks

This paper presented a novel computer vision based system that can track the movement of hundreds of model AGR core components in seismic tests. The bespoke motion capture software tool based on the LKOF algorithm has proven to be fit for purpose, being able to track all the components across the core array, at a resolution of 0.1mm. The level of confidence in the tracking outputs is high, as two independent vision systems (the HSV and the IRV) working in parallel show similar performance. Mapping the displacement response in an AGR core physical model is instrumental for understanding the core dynamics and for feeding experimental data for computer model validation. Without attempting to characterize the dynamic response of the core array in detail, it was shown how the tracking system can reveal patterns of response for certain component locations and orientations. Such findings can translate to the real AGR core behaviour and can contribute to the seismic assessments of distortion and/or key disengagement with implications on the control channel and fuel channel shapes. Future work will employ the tracking data in the validation of the existing numerical models for AGR seismic behaviour. The tracking tool and the tracking method are general in nature, hence they are transferrable to other case studies involving multi-body assemblies under dynamic loading.

Acknowledgement
The authors would like to thank EDF Energy for financial and technical support. The views expressed in this paper are those of the authors and do not necessarily represent those of EDF Energy.

List of Abbreviations
AGR: Advanced Gas-cooled Reactor
D: Focal Distance
DAQ: Data Acquisition System
DCB: Doubly Cracked Brick
FL: Focal Length
FOW: Field Of View
HSV:High Speed Video
IR: Infrared
LKOF: Lucas Kanade Tracking Algorithm
SLA: Single Layer Array
MLA: Multi Layer Array
UOB: University of Bristol
Z: Elevation of camera above the shaking table

References

Dihoru, L., Oddbjornsson, O., Brasier, S., Crewe, A.J., Taylor, C.A., Steer, A.G. (2015).*A single layer rig for exploring the dynamics of an advanced gas cooled reactor graphite core: commissioning and proposed validation studies.* In: Proc. of SECED Conference: Earthquake Risk and Engineering towards a Resilient World 9-10 July 2015, Cambridge UK.

Dihoru L., Oddbjornsson O., Kloukinas P., Dietz M., Horseman T., Voyagaki E, Crewe A.J., Taylor C.A. (2016), *The development of a physical model of an Advanced Gas Cooled Reactor core: Outline of the feasibility study,* Nuclear Engineering and Design 323 (2017) 269–279.

Dihoru L., Dietz M., Horseman T., Kloukinas P., Oddbjornsson O., Voyagaki E, Crewe A.J., Taylor C.A. (2018), *Neural networks for displacement analysis in an advanced gas cooled reactor core model,* Nuclear Engineering and Design 332 (2018) 252–266.

Flewitt and Wickham (2015) (eds), *Engineering Challenges Associated with the Life of Graphite Reactor Cores*, EMAS Publishing, ISBN-978-0-9576730-5-2.

Kelson R. T. Aires; Andre M. Santana; Adelardo A. D. Medeiros (2008). *Optical Flow Using Color Information.* ACM New York, NY, USA. ISBN 978-1-59593-753-7.

Koziara T and Bićanić N (2011), *International Journal for Numerical Methods in Engineering*, 87, 437–456.

Kralj B., Humphreys S. J., Duncan B. G. J. (2005), *Seismic Modelling of and AGR Nuclear Reactor Core,* Proceedings of the Ageing Management of Graphite Reactor Cores, University of Cardiff, 28-30 November, 193-200.

Kurihara K., Hoshino S., Yamane K., Nakamura Y. (2002), *Optical motion capture system with pan-tilt camera tracking and real time data processing,* Proceedings of the 2002 IEEE International Conference on Robotics 8 Automation, Washington, DC.

Lucas B.D., Kanade T. (1981), *An Image Registration Technique with an Application to Stereo Vision*, Proceedings of DARPA Image Understanding Workshop, 1981, pp. 121-130.

Motion Capture: Magnetic Systems (1995). Next Generation. Imagine Media (10): 51., October 1995.

Moeslund T.B., Granum E. (2001), *A Survey of Computer Vision-Based Human Motion Capture*, Computer Vision and Image Understanding 81, 231–268.

Nakamura Y., Yamane K., Kurihara K., Suzuki I. (2003), *Method of processing passive optical motion capture data,* US Patent No. US20030215130 A1, Application No. US 10/360,872.

Neighbour, G.B. (2007) (ed), *Management of Aging Processes in Graphite Reactor Cores,* RSC Publishing, Cambridge. ISBN-978-0-85404-345-3.

Neighbour, G.B. (2013) (ed), *Modelling and Measuring Reactor Core Graphite Properties and Performance,* RSC Publishing, Cambridge, ISBN-978-1-84973-390-8.

Rohas, R. (2010), *Lukas-Kanade in a Nutshell*, Report, Free University of Berlin, Dept. of Computer Science and Mathematics.

Roetenberg D., Luinge H., Slycke P. (2013), *Full 6DOF Human Motion Tracking Using Miniature Inertial Sensors*, Xsens MVN, © XSENS Technologies – version 3.

Sementille A.C., Lourenco L.E., Ferreira Brega J.R., Rodello I. (2004), *A motion capture system using passive markers,* Proceedings of the ACM SIGGRAPH International Conference on Virtual Reality Continuum and Its Applications in Industry., VRCAI'04, 440-447.

Stenborg E., Svensson L. (2005), *Complete Camera Calibration by Waving a Wand,* MSci Thesis, Department of Signals and Systems, Image Analysis Group, Chalmers University of Technology, Göteborg, Sweden.

Vlasic D., Adelsberger R., Vannucci G., Barnwell J., Gross M., Matusik W., Popovic J.(2007), *Practical Motion Capture in Everyday Surroundings,* ACM Transactions on Graphics (TOG), Proceedings of ACM SIGGRAPH 2007, Volume 26 Issue 3, July 2007.

Voyagaki, E, Kloukinas, P, Dietz, M, Dihoru, L, Horseman, T, Oddbjornsson, O, Crewe, AJ, Taylor, CA & Steer, A, (2018), *Earthquake response of a multiblock nuclear reactor graphite core: Experimental model vs. simulations,* Earthquake Engineering and Structural Dynamics, 47., 2601-2626